Influence of stenosis severity on hemodynamics flow at low Reynolds numbers: A computational fluid dynamic study

I. A. Fetuga[1], O. Oluwatusin[1], S. M. Abolarin[2], O. O. Olakoyejo[1], A. O. Adelaja[1], D. Z. Olaoye[1],
A. S. Adeleke[1], J. K. Gbegudu[1], K. S. Aderemi[1]

[1]Department of Mechanical Engineering, University of Lagos, Akoka, Lagos, Nigeria.
[2]Department Engineering Sciences, University of the Free State, Bloemfontein, Free South Africa

---

ABSTRACT: The restriction of blood flow due to narrowing of arteries that supply blood to different parts of the body leads to high blood pressure and cholesterol in humans. In this study, blood flow in a 3D model of arterial stenosis was examined using computational fluid dynamics (CFD) technique. The geometry of the stenosis was modeled using ANSYS software, and a structured tetrahedral mesh was generated for accurate representation. The CFD analysis was performed using the ANSYS (FLUENT) 19.2 commercial code to investigate three stenosis levels of 75%, 50%, and 25% over the Reynolds number range of 500-2000 with blood as the working fluid. The blood flowed steadily upstream of the stenosis as incompressible, homogeneous, and Newtonian, while the artery is considered to be inflexible. The Reynolds-averaged Navier-Stokes equations and the low Reynolds number SST k-ω turbulence model were employed to simulate the blood flow. The governing equations are solved, and the pressure-velocity coupling is handled using the SIMPLEC algorithm. The steady state velocity and pressure generated at the inlet and outlet of the artery enabled the hemodynamic properties and flow reversal through arteries with a progressive amount of atherosclerosis to be determined. The results are presented in terms of velocity distribution, streamlines, and turbulence intensity contours. The results showed that at the throat (Z = 0) of the 75% stenosis, the relative magnitude of the velocity is greater than or equal to four times the average velocity. Reversal of flow is visible at $1.5D \geq z > 6D$ for Re = 500 and $1.5D \geq z \leq 4D$ for Re = 750 and Re = 2000. Furthermore, the effects of 25% stenosis on the flow pattern are relatively blunt and weak at $Re < 2000$. The throat of the stenosis, or a site therein, exhibits the highest value of centerline velocity, while turbulence intensity becomes severe at the post-stenotic site and they both increase with increasing stenosis level. The study provides valuable insights into the velocity distribution, flow reversal phenomenon, and turbulence intensity in arterial stenosis. The findings highlight the significant impact of stenosis levels and Reynolds numbers on the hemodynamic behavior, offering important considerations for understanding and managing arterial health issues.

KEYWORDS: Cardiovascular diseases, CFD, Flow disturbance, Hemodynamic flow, Stenotic arteries

[Received Feb. 8, 2023; Revised July 14, 2023; Accepted Aug. 1, 2023] Print ISSN: 0189-9546 | Online ISSN: 2437-2110

Nomenclature

D	[mm]	Diameter of the artery
G	[-]	Mesh size
h_s	[mm]	Maximum height of the stenosis at throat
L	[mm]	Length of the artery
Ls	[mm]	Maximum width of the stenosis
L_h	[mm]	Hydrodynamic length
R	[mm]	Radius of the artery
Re	[-]	Reynolds number
v	[m/s]	Velocity
ρ	[kg/m^3]	Blood density
μ	[pa.s]	Blood viscosity

I. INTRODUCTION

Cardiovascular diseases (CVDs) have been the major cause of death in the present day. They are basically types of diseases responsible for the abnormal functioning of the blood vessels. According to data from the World Health Organization, 17.1 million people died from CVDs in 2004, accounting for close to 29 percent of all deaths (WHO, 2009). As 82 percent of all deaths worldwide in 2004 were recorded in under-developed nations, these nations were more vulnerable to CVDs (WHO, 2009). Projected World Health Organization figures show that the mortality curve of CVDs is still rising, and by the end of 2030, 23.6 million individuals are anticipated to pass away from these conditions due to heart attacks, or strokes (WHO, 2009).

Researchers have looked into a number of studies on stenotic flow, particularly in the vicinity of stenosis, because of its intriguing characteristics and the clinical implications from a fluid dynamic perspective.

On the basis of the flow condition that manifests in the circulatory system as a function of artery diameter and at a low Reynolds number range (Re), (Ahmed and Giddens, 1983a)

*Corresponding author: fetugaebraheem@gmail.com

doi: http://dx.doi.org/10.4314/njtd.v18i4.1621

employed laser Doppler anemometry at Reynolds numbers 500-2000 to visualize flow in the upstream and downstream of the stenosis under conditions of steady state. It was revealed from their results that at 75% stenosis severity, flow is in the turbulence transition region. More specifically, as the Reynolds number elevated from 500 to 1000, a growth in the recirculation zone was reported. (Ahmed and Giddens, 1984) took their research beyond the steady state by examining the circulatory system under the pulsatile flow condition for Re varying from 200 to 1000. It was discovered from their findings that for low Re, the flow disturbance intensity is significantly larger towards the wall than in the center of the artery. This evidently shows that the turbulence first occurs at the shear layer and further radiates inwardly to the center of the artery by increasing Re.

Several numerical models have been adopted to mimic actual hemodynamic flow. (Varghese, Frankel and Fischer, 2007a, 2007b) employed a direct numerical simulation study to corroborate the experimental findings of Ahmed and Giddens for axisymmetric stenosis of 75%. The investigation was further extended for asymmetric stenosis with a similar degree of stenosis under the conditions of steady and pulsatile flow. (Ryval, Straatman and Steinman, 2004) used a computational approach to imitate the experimental work of (Ahmed and Giddens, 1983b, 1984) under steady and pulsatile state flow conditions. The results found that the transitional k-w turbulence model provided better results than the standard k-w turbulence model for steady and pulsatile flows. (Dietiker and Hoffmann, 2006) employed a computational approach to compare Newtonian and Non-Newtonian flow characteristics in a tapered artery with different levels of stenosis.

The study revealed that during peak systole, an area reduction of 75% stenosis damages the endothelium layer. (Banks and Bressloff, 2007) investigated the reliability and accuracy of both the RNG $k-\varepsilon$ turbulence model and the transitional $k-\omega$ turbulence model. Two significant differences were reported between the turbulence models and further concluded that the transitional $k-\omega$ model turbulence more accurately describes flow phenomena better. (Liao, Lee and Low, 2011) examined stenotic vessels subject to simple and physiological unsteady flow conditions. This was investigated by comparing both flow conditions at all phases of the flow cycle, they concluded that flow deceleration was the cause of vortex translation and formation. (Mittal, Simmons and Najjar, 2003) performed a LES study for Reynolds number 750 to 2000 under the pulsatile flow condition on the two-dimensional geometry having occlusion of semi-circular structure on one of it sides. From their results, it was found that as the Re rises, the intensity of the turbulence kinetic energy and specific dissipation grow in the vicinity of the stenosis. (Albadawi *et al*., 2021) predicted stenotic areas in carotid arteries using computational fluid dynamics (CFD). They developed a patient-specific blood flow model and investigated WSS and velocity distribution. From their results, WSS increased considerably with stenosis severity near the arterial bifurcation (location 1), but decreased further away (position 2). And Based on WSS and oscillatory shear index (OSI) measurements, the artery bifurcation was identified as a high-risk region for thrombus development and arterial wall rupture. (Zhao *et al.*, 2021) assessed the hemodynamics in a microfluidic model of thrombosis with stenosis. They utilized an advanced CFD simulation method to accurately map the distribution of shear rate and wall shear stress in the stenotic region. The findings indicated that the level of stenosis played a crucial role in determining the distribution of the shear rate and wall shear stress, while the contraction angle had a significant impact on the distribution of shear rate gradient. Additionally, the study examined viscosity effects using a Generalized Power-Law model, which showed minimal differences in the shear rate distribution when compared to Newtonian simulations with a water medium. (Amir et al., 2022) investigated the spatiotemporal flow hemodynamics in a stenosed artery. They explored pulsatile flow hemodynamics in a variety of stenosed vessels and discovered primary, secondary, and tertiary vortices. Vortex size and strength rose with Re and stenosis severity, but decreased with greater activity (Womersley number, Wo). In a 50% obstructed artery, their results showed that atherosclerosis was promoted for Re = 500 and suppressed for Re = 800. Reduced flow and strong oscillations in wall shear stress (TAWSS) and oscillatory shear index (OSI 0.5) were seen in a 75% severity case, favoring plaque fissure at Re = 800. At Re = 800, similar triggering events were observed in a 50% obstructed artery with subsequent stenosis. (Dabagh, Vasava and Jalali, 2015) studied pulsatile blood flow in a three-dimensional model of the human thoracic aorta to investigate the effects of atherosclerotic lesion growth, plaque location, and peripheral symmetry. Vulnerable areas with different degrees of stenosis severity (50% and 80%) were analyzed. The study revealed that the magnitude and distribution of wall shear stress (WSS) were strongly influenced by plaque size, symmetry, and location. The results identified sites susceptible to early atherosclerosis and showed WSS values exceeding 50 Pa at the throat of 80% stenosed left common carotid and brachiocephalic arteries. (Ferdows *et al.*, 2023) investigated how wall shear stress indicators influence hemodynamic conditions in coronary main arterial diseases. The study used patient-based coronary artery models from CCTA imaging and CH simulations. Results, including velocity magnitude, wall shear stress, and computational fractional flow reserve, predicted the severity of coronary diseases effectively. (Hoque *et al.*, 2021) investigated the impact of hemodynamic factors on detecting atherosclerotic severity in coronary main arteries, including single and multiple sequential stenosis cases. Pulsatile heart flow simulations are used to analyze hemodynamic properties such as wall shear stress (WSS) and velocity magnitude (VM) in patient-based right coronary artery models of MCS. The study reveals a relationship between proximal moderate stenosis and distal severe stenosis models based on different degrees of stenosis. (Molochnikov *et al.*, 2022) performed a unique experimental investigation and direct numerical simulation to examine the steady flow in a channel branching zone, precisely simulating the femoral artery proximal anastomosis. They concentrated on the Reynolds number (Re) of 1500, which represents the maximal blood flow during heart contractions. The analysis uncovered regularities in the flow structure development throughout the main channel and branch region, with a focus on flow separation zones. Notably, their investigation confirmed the presence of secondary flows within these separation zones and also identified the exact flow rate ratio ranges that resulted in the emergence of flow turbulence indications in the mixing layer at the interface between these regions. (Changsheng *et al.*, 2023) studied the effect of anatomical structure on hemodynamics in iliac vein stenosis, as well as techniques to reduce in-stent thrombosis. Vascular models with varied degrees of stenosis, taper angles, and tilt angles were examined using in vitro investigations and computational fluid dynamics (CFD). The results revealed increased wall shear stress (WSS) at the stenosis site, boosting the likelihood of thrombosis. Small tilt angles heightened the effects of the vascular wall. (Albadawi *et al.*, 2023) investigated turbulence flow models in coronary artery stenosis. Their study aimed to find the most accurate turbulence flow model by comparing numerical simulations with experimental data. Laminar flow and K-ε, and large eddy simulation (LES) turbulence models were evaluated. Their findings showed laminar and LES models performed better in simulating blood flow than the turbulence model. (Mirfendereski and Park, 2022) created a 3D numerical simulation of pulsatile flow in a stenotic channel using an immersed boundary approach to simulate blood flow in major arteries at Reynolds values of 750 and 1000. Flow physics and hemodynamic parameters based on wall shear stress (WSS) were investigated. Their results revealed that the downstream turbulent properties of the twin stenotic channel made it susceptible to atherosclerosis progression. As the degree of stenosis increased, so did the number of locations with non-physiological WSS-based characteristics.

This pioneering research offers a unique and insightful investigation into the complex hemodynamic flow through arterial stenosis. By considering varying stenosis severity and low Reynolds numbers, the study presents a comprehensive understanding of flow behavior within constricted arteries. Leveraging computational fluid dynamics (CFD) techniques, the research provides credible and precise insights into intricate flow patterns, including jet formations, flow separations, recirculation zones, and low-velocity layers at different axial distances.

A notable aspect of this study is its rigorous exploration of the influence of Reynolds numbers on flow dynamics, a critical factor often overlooked in low Reynolds number scenarios, particularly in the context of real-world physiological conditions. The identification of flow reversal and turbulence intensity in the post-stenotic region is particularly noteworthy and may hold significant implications for medical professionals and researchers in the cardiovascular field.

Through its interdisciplinary approach, integrating principles from both medical and engineering domains, this research sets a precedent for future investigations and contributes to the advancement of cardiovascular health research. The depth and breadth of its findings establish a strong foundation for further exploration and potential applications in targeted treatment strategies, ultimately leading to improved patient outcomes.

II. METHODOLOGY

A. *Geometry Description*

The 2D and three-dimensional models with the specified dimensions and geometry for the simulation are shown in Figures 1(a)-(b). These models are modified from the work of (Ahmed and Giddens, 1983b). The geometry was created using Design Modeler (ANSYS). In this study, the artery was modeled as a uniformly sized, smooth, three-dimensional tube, while the stenosis was assumed to have a Gaussian profile and be axisymmetric. Figure 1 illustrates the blood flow in an artery with a diameter (D) and a length (L) along the z-axis. To ensure complete flow development after a 4D entry length before the stenosis, a 20D outlet length is considered adequate, as determined using the hydrodynamic length expression (Lh = 0.05ReD).

The Gaussian profile is expressed by Eqn. (1).

$$R(z) = \begin{cases} R - \frac{h_s}{2}\left(1 + \cos\left(\frac{\pi z}{L_s}\right)\right) & |z| \geq L_s \\ R & |z| \leq L_s \end{cases} \quad (1)$$

Where L denotes the length of the artery, L_s represents the maximum width of the stenosis, h_s indicates the maximum height of the stenosis at the throat and R represents the radius of the unobstructed channel.

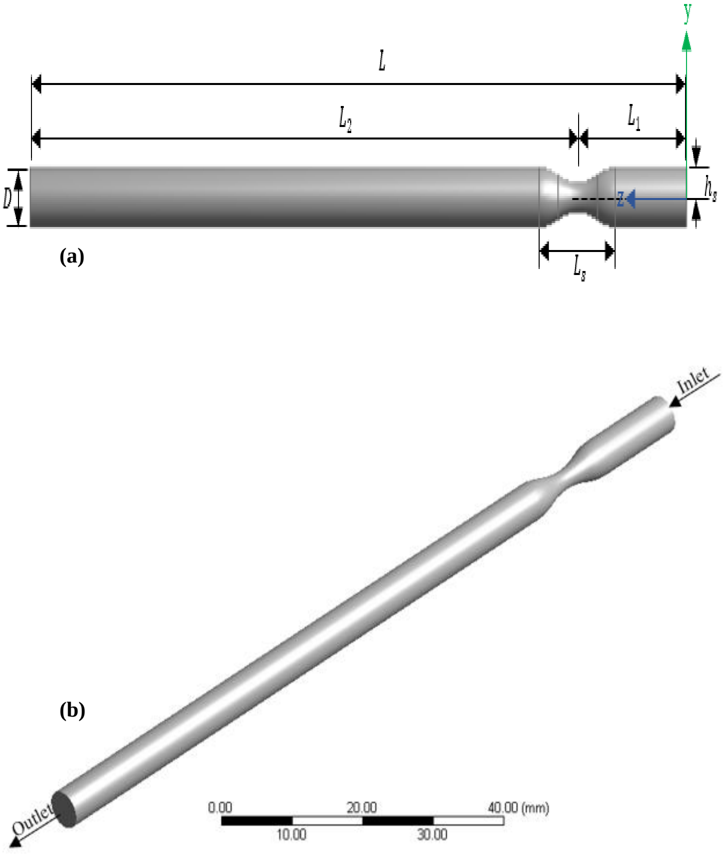

Figure 1. The schematic of a 75% stenotic vessel in (a) 2D with dimensions and (b) 3D

B. *Grid Generation*

The geometry was meshed using the Meshing feature within the ANSYS software package. Specifically, a patch conforming tetrahedral mesh with a structured approach was employed for the geometry. Understanding the flow profile around the stenosis and close to the walls is of utmost importance. To enhance the accuracy of measurements at the model's periphery, the walls were inflated, and a fine high-density mesh was applied to the geometry. For smooth transitions between mesh cells, the mesh's smoothing setting was set to high. Moreover, the geometry underwent further refinement with numerous divisions at the faces to comprehensively capture the boundary layer flow. The equiangle skewness was found to be below the acceptable criteria value of 0.98.

Table 1 Geometry parameter

Parameter	Dimension
$\boldsymbol{L}$	$24D$
$\boldsymbol{D}$	D^*
$\boldsymbol{R}$	$D/2$
$\boldsymbol{h_s}$	$0.25D, 0.15D, 0.067D$
$\boldsymbol{L_s}$	$2.8D$
$\boldsymbol{L_1}$	$4D$
$\boldsymbol{L_2}$	$20D$

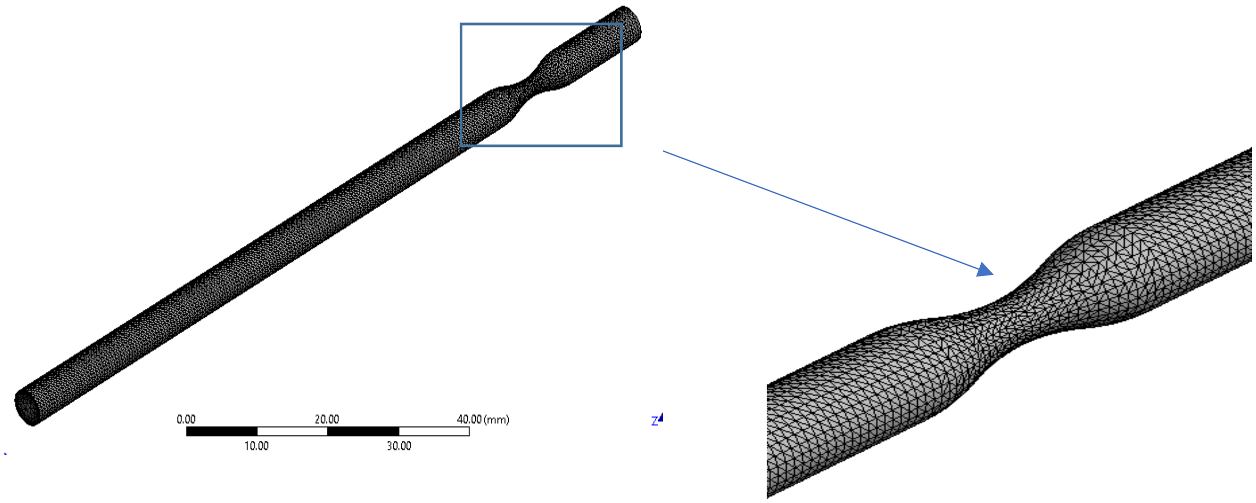

Figure 2. (a) the orthogonal view of structured grids for 75% stenosis and (b) the inset of structured grids for 75% stenosis site.

C. *Mathematical Formulation*

The governing equations used in the problem are described in this section. Navier-Stokes and continuity equations were employed to demystify the flow equations in this study. Using the same geometry configuration in Figure 1(a)-(b), the cylindrical polar coordinate system (r,θ,z) is used to represent the point in domain, where r, θ,and z denotes radial, circumferential and axial direction, respectively. The flow variation is independent of θ due to the axisymmetry. The assumptions made to simplify the analysis are listed below:

(1) The flow is 3D incompressible and steady.
(2) The ratio of the diameter of a red blood cell to the large artery diameter is insignificant. Thus, it is possible to disregard the two-phase flow.
(3) Blood flow is considered Newtonian.
(4) Artery is considered a rigid wall.
(5) No-slip at the solid-fluid interface
(6) The flow is fully developed.
(7) Gravitational and magnetic force are neglected.

The governing equations are as follow:

Navier-Stokes equation can be defined by

$$\frac{\partial u_i}{\partial x_i} = 0 \tag{2}$$

$$\frac{\partial u_i}{\partial t} + u_j \frac{\partial u_i}{\partial x_j} = \frac{-1}{\rho}\left(\frac{\partial P}{\partial x_i}\right) + \upsilon \frac{\partial^2 u_i}{\partial x_j \partial x_i} \tag{3}$$

Standard k -w Turbulence Model

Instantaneous component variables are given below

$$\begin{aligned} u &= \bar{u} + u', \\ v &= \bar{v} + v', \\ w &= \bar{w} + w', \\ p &= \bar{p} + p' \end{aligned} \tag{4}$$

Some necessary algebraic simplifications are performed on Navier-Stokes equations by taking the time-average with the aid of instantaneous component variables in Eqns. (3-4) to obtain a modified Navier-Stokes equation, which also known as Reynolds averaged Navier-Stokes (RANS) equations.

Reynolds average Navier-Stokes equations obtained are;

$$\frac{\partial}{\partial t}(\rho u_i) + \frac{\partial}{\partial x_j}(\rho u_i u_j) = -\frac{\partial P}{\partial x_i} + \frac{\partial}{\partial x_j}(2\mu s_{ij}) \tag{5}$$

where s_{ij} (strain-rate tensor) is expressed as;

$$s_{ij} = \frac{1}{2}\left(\frac{\partial u_i}{\partial x_j} + \frac{\partial u_i}{\partial x_i}\right) \tag{6}$$

Two equations, low Re $k - \omega$ turbulent model is introduced to the equations above in order to the solve eddy viscosity that arises from the transition from laminar to the turbulent flow.

The two-equation turbulence model are defined by;

$$k-equation; \quad \frac{\partial}{\partial t}(\rho k)+\frac{\partial}{\partial x_i}(\rho k u_i)=\frac{\partial}{\partial x_j}\left(\Gamma_k \frac{\partial k}{\partial x_j}\right)+G_k-Y_k$$

$$\omega-equation; \quad \frac{\partial}{\partial t}(\rho \omega)+\frac{\partial}{\partial x_i}(\rho \omega u_i)=\frac{\partial}{\partial x_j}\left(\Gamma_\omega \frac{\partial \omega}{\partial x_j}\right)+G_\omega-Y_\omega \tag{7}$$

where, k denotes turbulence kinetic energy, ω represents specific dissipation rate, Γ_k, Γ_ω are effective diffusivity term, and G_k, G_ω are generation term, Y_k, Y_ω are destruction term

$$\Gamma_k=\mu+\alpha^*\left(\rho\frac{k}{\omega}\right)\frac{1}{\sigma_k} \tag{8}$$

$$\Gamma_\omega=\mu+\alpha^*\left(\rho\frac{k}{\omega}\right)\frac{1}{\sigma_\omega} \tag{9}$$

The standard k-ω turbulence model is basically determined by Reynolds number correction factor which are defined by;

$$\alpha^*=\alpha^*_\infty\left(\frac{\alpha^*_0+\frac{Re_t}{Re_k}}{1+\frac{Re_t}{Re_k}}\right)$$

$$G_k=-\rho\bar{u}_i\bar{u}_j\frac{\partial u_j}{\partial x_i}$$

$$G_\omega=\alpha\left(\frac{\omega}{k}\right)G_k$$

$$\alpha=\frac{\alpha_0}{\alpha^*}\left(\frac{\alpha_0+\frac{Re_t}{Re_\omega}}{1+\frac{Re_t}{Re_\omega}}\right)$$

$$Y_k=\rho\beta^* f_{\beta^*}k\omega\ , \quad \beta_i^*=\beta^*_\infty\left[\frac{0.2666+\left(\frac{Re_t}{R_\beta}\right)^4}{1+\left(\frac{Re_t}{R_\beta}\right)^4}\right] \tag{10}$$

Closure coefficient for $k-\omega$ turbulent model

$$\alpha^*_\infty=1,\ \alpha_\infty=0.52, \alpha_0=0.1111, \beta^*_\infty=0.09, \beta_i=0.072, R_\beta=8,\ R_k=6,\ \ R_w=2.95,\ \xi^*=1.5\ \ M_{t0}=0.25\ \ \sigma_K=2.0\ \ \sigma_w=2 \tag{11}$$

The boundary conditions applied at the inlet, outlet, and wall of the arteries are summarized in Table 2, while the fluid properties of the blood as well as the artery are summarized in Table 3.

Table 2. Boundary Conditions

Boundary	Location	Condition
	At $r=R(z)$	$v_r=v_z=0$ (No slip)
	At $r=R(z), v_z=0$	$\frac{\partial v_z}{\partial z}=0$ no shear along the central axis of the tube
Inlet	at $z=0, v_r=0$	$v_z=v_{max}(1-\frac{x^2+y^2}{r^2})$
Outlet	At $z=L$	$\frac{\partial v_r}{\partial z}=\frac{\partial v_z}{\partial z}=0$
Turbulent Boundary Conditions		
Hydrodynamic	Turbulence intensity	$I=0.16\left(Re_{nf}\right)^{-\frac{1}{8}}$
	Length scale	$l=0.07D_h$
	Turbulence viscosity ratio	$\frac{\mu_t}{\mu}$

Where,

$$\boldsymbol{v_{max}=2v_{avg}} \tag{2}$$

$$\boldsymbol{Re=\frac{\rho v_{avg}D}{\mu}} \tag{33}$$

Table 3. Physical properties

Properties	$\boldsymbol{\rho(kg/m^3)}$	$\boldsymbol{\mu(kg.m/s)}$
Blood	1050	0.003675
Arterial wall	1075	-

III. NUMERICAL PROCEDURE

The continuity and Navier-Stokes equations, guided by specific assumptions and corresponding boundary conditions, were numerically solved using the commercial CFD software package, ANSYS (FLUENT) 19.2. To ensure accurate and stable pressure-velocity coupling, the study employed the robust SIMPLEC (Semi-Implicit Method for Pressure-Linked Equations) Algorithm. For numerical discretization, a carefully chosen scheme was adopted. Specifically, a Gauss cell-based approach was used for gradient calculations, providing accurate representations of spatial variations. Additionally, to handle pressure terms and momentum equations, a second-order upwind scheme was implemented. These discretization choices were made to ensure precision and reliability in the simulation, effectively capturing the intricacies of the fluid flow behavior under investigation. Furthermore, a turbulence model specifically designed for low-Reynolds number flows, the SST k-ω turbulence model, was incorporated. This choice ensures an accurate representation of turbulence effects, which play a significant role in many fluid flow scenarios. To ascertain the credibility of the numerical solutions, rigorous convergence criteria were established. By setting the convergence threshold to 1×10^{-7} fo(1) all the governing equations, the simulation aimed to achieve a high level of precision and stability in capturing the fluid flow behavior. These criteria serve as essential benchmarks to ensure the reliability and validity of the results obtained from the computational analysis.

IV. RESULTS AND DISCUSSION

A. Grid Independence Analysis

A grid sensitivity study was conducted to avoid the cumbersome and excessive number of grids in order to save computational time and cost. Nine different mesh sizes (see Figure 3), denoted by G1, G2, G3, G4, G5, G6, G7, G8, and G9 are presented according to the ascending order of elements and nodes. Figure 3 shows the grid independence test, it compares the centerline velocity at different mesh sizes for the case of 75% stenosis at a Reynolds number of 500. The grid independence test result indicates that making the grid finer from G4 to G9 does not show a significant change in centerline velocity (when rounding up to five decimal places) within the mesh size (G4 - G9). Thus, the grid G4 (element-119515) is chosen for this computational study based on accuracy, computational time, and cost.

B. Validation and Verification of Model

To further verify the consistency and accuracy of the model adopted, the numerical solutions of this study plotted the dimensionless velocity profile as a function of the dimensionless radial distance and were compared with the experimental results and the available numerical results documented in the literature. Geometry similar to the experimental one (a case of 75% stenosis at an axial distance of z=1D and z=2.5D at Reynolds number of 500) has been considered for the validation. As shown in Figures 4 and 5, the dimensionless velocity profile plotted against the dimensionless radial distance at axial sites when z= 1D is shown in Figure 4, while Figure 5 shows when z=2.5D. In these figures, the results of the present study were compared with the experimental data from the work of (Ahmed and Giddens, 1983b) and numerical data from the work of (Varghese, Frankel and Fischer, 2007a). The dimensionless radial distance reduces from 1 to 0.8, when the dimensionless velocity was negative.

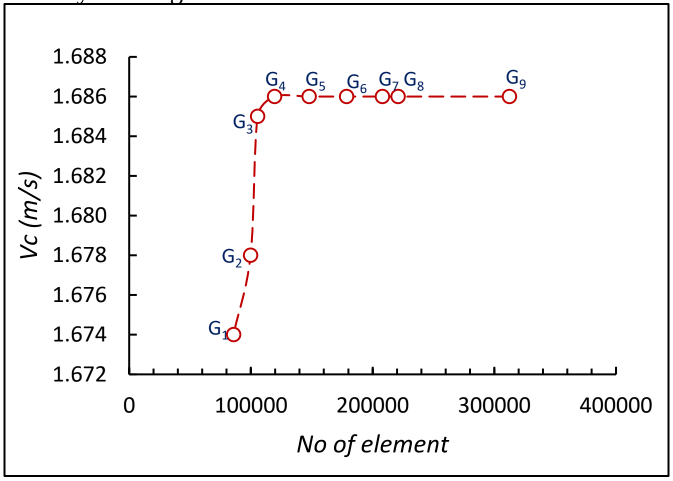

Figure 3. Grid Independence Test

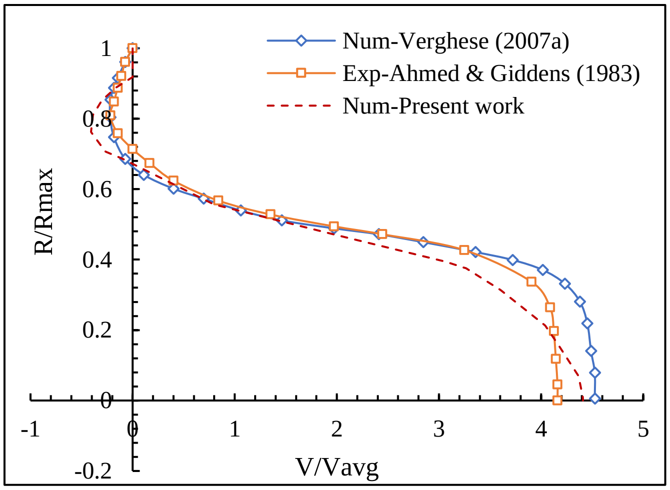

Figure 4. Dimensionless velocity profile for 75% stenosis at axial site $\bar{Z} = 1.0$ at $Re = 500$

The recorded transition profile indicates a reduction in dimensionless radial distance from 0.8 to approximately 0.3 as the velocity increased from -0.3 to 4.2. Beyond a velocity ratio of 4, the radial distance decreased sharply, suggesting the formation of a jet when blood flow passes through the stenosis. Additionally, the relative magnitude of velocity was observed to be four times greater than the mean velocity. Consequently, a larger stenosis would necessitate the heart to perform more work to circulate blood past the obstruction. Furthermore, the validation process demonstrated a reasonable correlation between the numerical solutions obtained in the current study and those provided by Ahmed and Giddens, compared to the numerical results from (Varghese, Frankel and Fischer, 2007a). This agreement with existing literature instills confidence in the accuracy of the numerical model employed in this research.

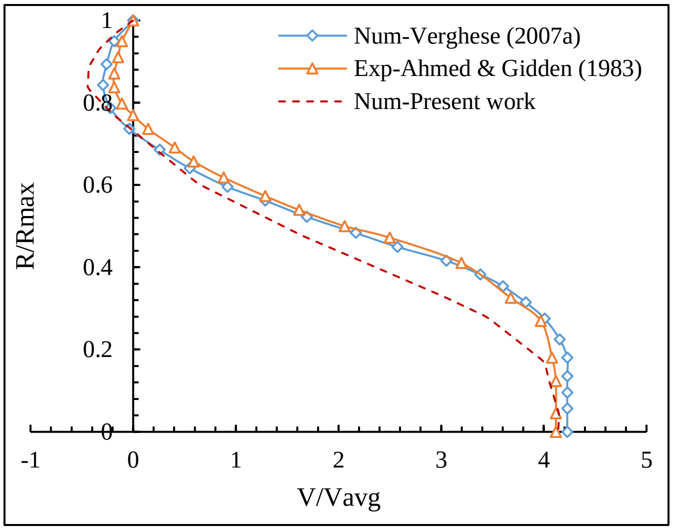

Figure 5. Dimensionless velocity profile for 75% stenosis at axial sites $\bar{Z} = 2.5$ at Re=500

C. *Influence of Reynolds number*

For the 75% stenosis, velocity profiles were obtained at six axial sites for $Re = 500, 750,$ and 2000. The results for the stated Reynolds number are presented in Figure 6(a)-(b). At $\bar{Z} = 0$, when the flow passes through the stenosis, it is obvious that at the throat a jet formation occurs, and the relative magnitude of the velocity is approximately four times greater than the value of the average velocity. Figure 6(a) shows that no flow separation is visible as a result of the variation in Reynolds number. Flow separation with variation in Reynolds number becomes visible at $\bar{Z} = 1.5$ distal to the constriction for all three Reynolds numbers, which are well conformed to the experimental data. For $Re = 500$, the flow reversal was seen to extend as far as $\bar{Z} = 3.7$ (Figure 6(d)) and continues well beyond axial site $\bar{Z} = 6$ (Figure 6(f)) with the flow downstream of the 75% stenosis reattaching at $\bar{Z} = 15$. (Varghese, Frankel and Fischer, 2007a) reported similar findings and asserted that flow does not reattach until $\bar{Z} = 16$.

For both $Re = 750$ and $Re = 2000$, early flow separation zone occurs at $\bar{Z} = 1.5$ (Figure 6(b)) and finally re-attached at $\bar{Z} = 3.7$ (Figure 6(e)). It is revealed that for all cases of the Reynolds number adopted in this study, the recirculation length zone reduces with increasing axial distance before flow completely reattaches to the wall. It is critical to note the layer of low velocity for all the Reynolds numbers at axial stations. A very thin layer of low velocity is found at the throat ($z = 0$) of the stenosis, as shown in Figure 6(a). Distal to the stenosis, at an axial site of $1.5D$ to $3.7D$, a very similar and moderate layer of velocity is seen as displayed in Figure 6 (b)-(e).

Meanwhile, far downstream of stenosis at $z = 6D$, a very thick low velocity layer corresponding to Reynolds number 500 is evidently seen. The axial station $z = 6D$, as shown in Figure 6(f) is a point to critically note. This could be attributed to the flow reattachment at an axial distance $5 < \overline{Z} < 6$ for $Re = 750$ and 2000 (Ahmed and Giddens, 1983b). In a nutshell, the presence of high-velocity jets, flow separation, and recirculation zones at different Reynolds numbers underscores the importance of considering stenosis severity and Reynolds number in the assessment of blood flow behavior in stenosed arteries. This understanding is crucial for studying and potentially managing conditions related to arterial narrowing in the human body.

D. Influence of Degree of Stenosis

Figures 7 and 8 present the impact of the severity of the area reduction on the flow stream for stenoses of 25% and 75% at Re of 500 and 2000, respectively for different values of z. Axial velocity profiles at five axial sites are obtained. In Figure 7, for the case of 25% stenosis, although the effects of the area reduction on the flow field are significantly weak and blunt at all the axial stations, the formation of a shear layer with a point of inflexion in the velocity profile can be clearly seen, it remains laminar and stable, and no separation of flow was observed at all the six five axial sites investigated for *Re*=500.

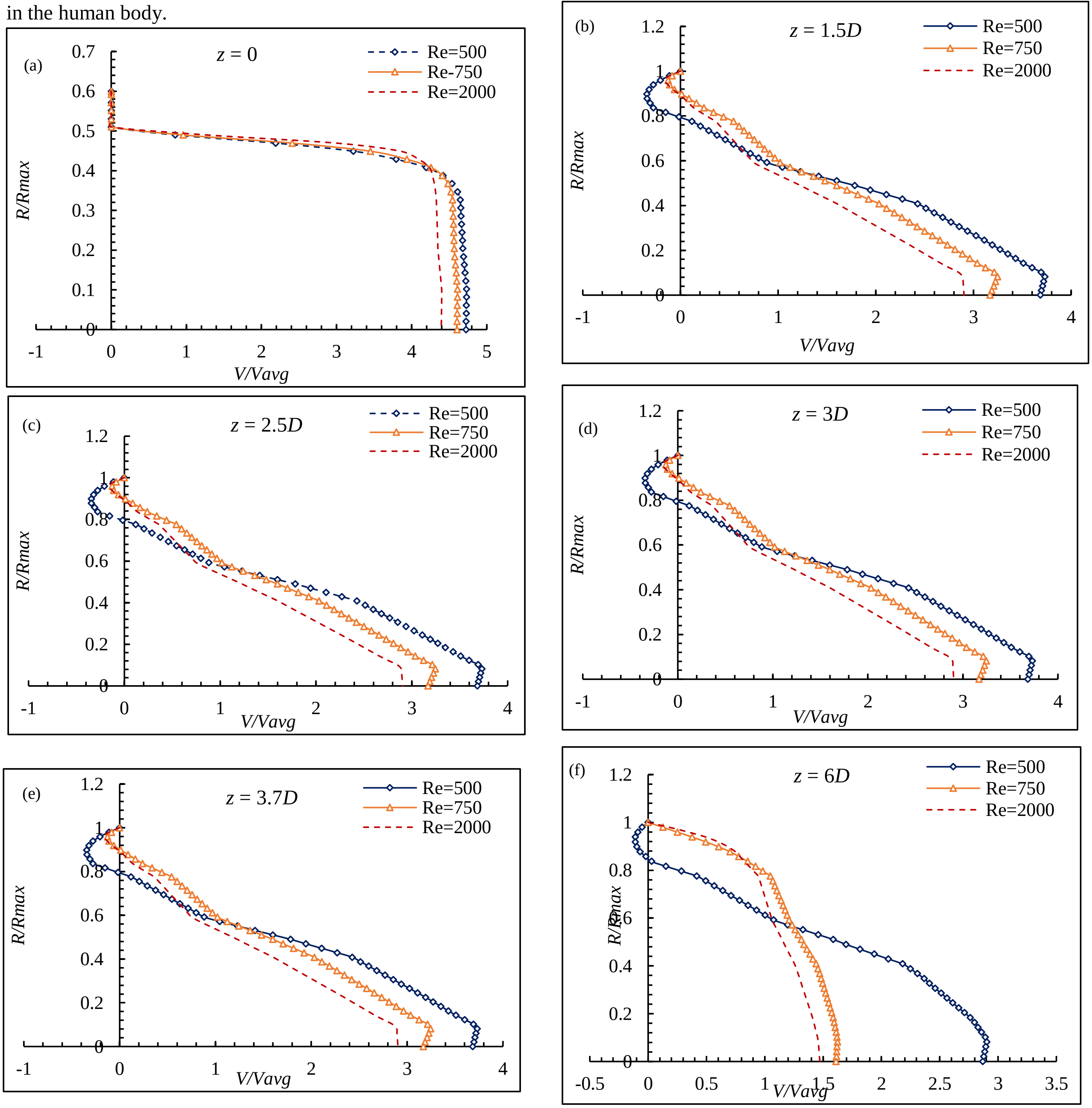

Figure 6. Dimensionless radial distance as a function dimensionless velocity profile for 75% stenosis at axial site (a) *z* = 0, (b) *z* = 1.5*D*, (c) *z* = 2.5*D*, (d) *z* = 3.0*D*, (e) *z* = 3.7*D* and (f) *z* = 6*D*.

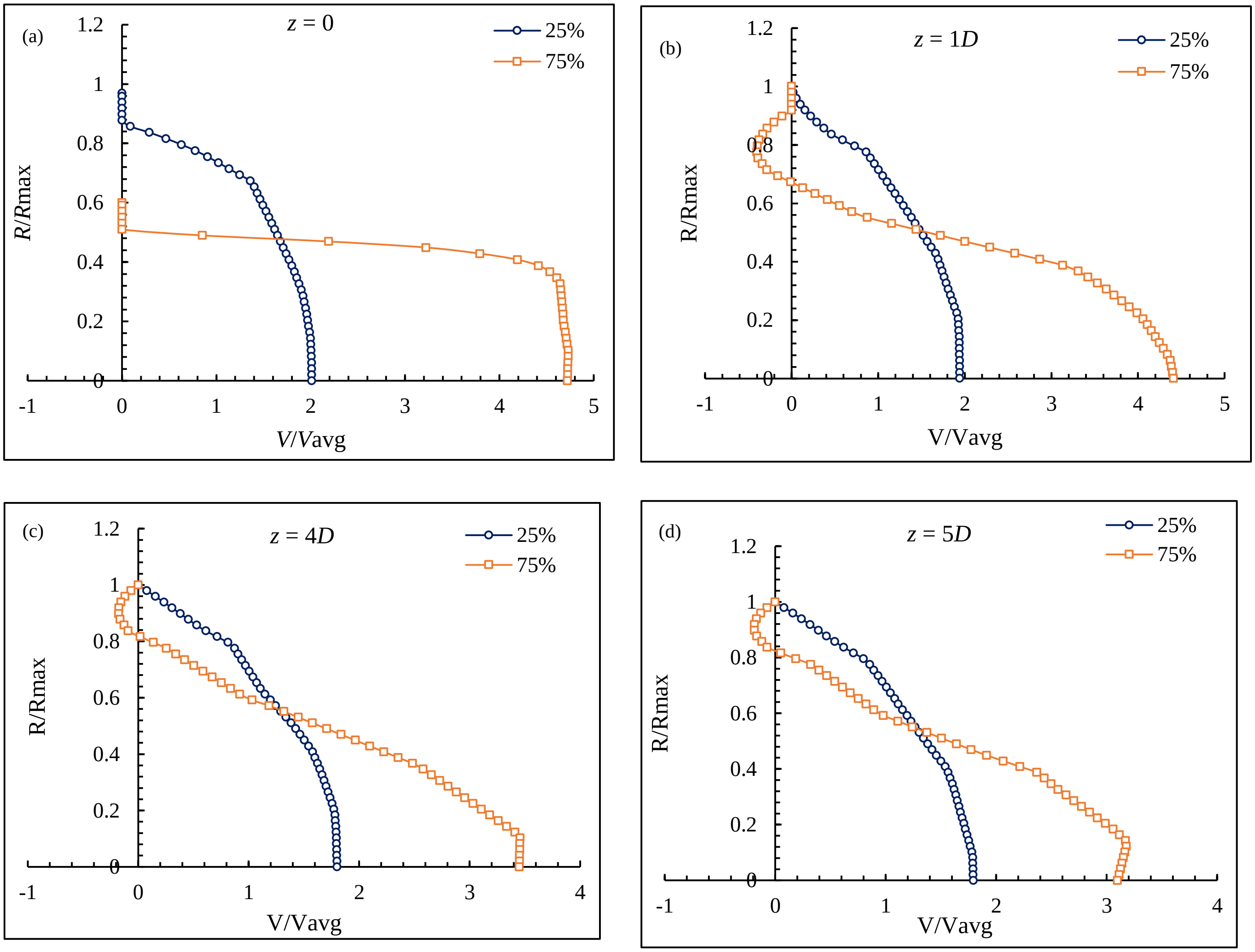

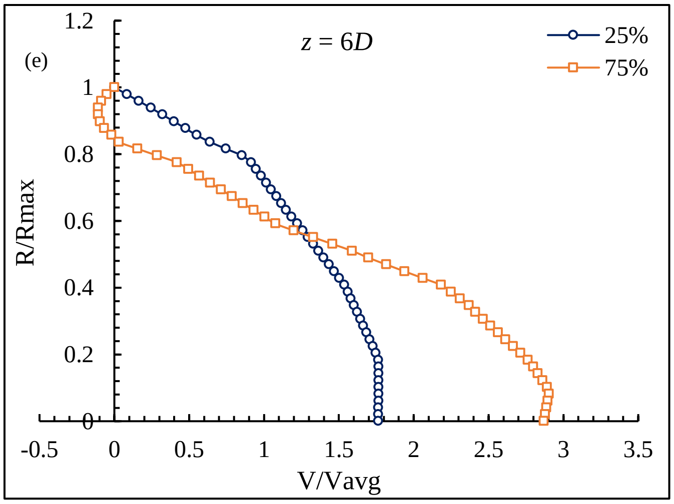

Figure 7. Dimensionless velocity profile for 25% and75% stenosis at axial site (a) *z* = 0, (b) *z* = 1*D*, (c) *z* = 4*D*, (d) *z* = 5*D*, (e) *z* = 6*D* at Re = 500.

At a stenosis of 75% as shown in Figure 7, as the blood circulated through the stenosis at Re = 500, when z = 0, no recirculation was found. However, as the value of z becomes 1D, recirculation was observed to commence at a dimensionless radial distance of 0.84 and continues to exist till z=6D. However, at z= 1.0D and *Re* = 2000 (Figure 8) bluntly negative velocity was found near the wall, which basically illustrates the exhibition of a small recirculation zone. Furthermore, for this case of studied stenosis for Reynolds numbers of 500 and 2000 at all axial sites, the flow behavior at the throat and downstream of the stenosis is very stable and shows no form of flow disturbance. For a 75 % stenosis, the velocity profiles at Re = 500 depict a flow recirculation zone and a thick layer of low velocity fluid starting from an axial site z=1D up to far downstream of the stenosis. It is also observed that the flow does not reattach at the axial site z=6D but exists beyond this axial distance. However, the flow separation zone increases as the Reynolds number increases. The findings closely resemble those reported in a study conducted by (Deshpande, Giddens and Mabon, 1976). Flow separation is observed at a dimensionless distance of 1D < z ≤ 4D for Re=2000, and it eventually re-attaches when z=4D.

E. *Centreline velocity*

Figures 9(a) to 9(c) compare axial centerline velocity comparisons for 25%, 50%, and 75% area reduction for Reynolds numbers 500, 1000 and 2000, respectively. When flow passes through the throat, a noticeable increase in the centerline velocity (v_c) is seen close to or at the neck of the stenosis. For these range of Reynolds numbers (500 (Figure 9(a)), 1000 (Figure 9(b)), and 2000 (Figure 9(c)), at 25% stenosis, the Re = 500 has the lowest centerline velocity of 0.66 and this is as a result of its very mild minimum area reduction and possibly lease flow rate. Variation in flow behavior exists as it further proceeds downstream of the stenosis. As degree of stenosis is increased to 50%, further increase in centerline velocity to about 0.89 is observed in Figure 9(a) at the Re = 500 and it continues to increase to 1.71 as the Re was increased to 1000 and then to 3.34 as the Re was increased to 2000. Similarly, flow behavior with rapidly increased centerline velocity is experienced in 75% stenosis at the different Reynolds numbers. However, as predicted, the greatest rise in the v_c with value of 6.2 is recorded for Re = 2000 close to the neck of the stenosis (Figure 9(c)), with values ranging from the largest for a stenosis of 75% to the smallest for a stenosis of 25%. In all the cases, the transition to turbulence is evident at $\overline{Z} \geq 5$, but it occurs earlier in both Re=1000 and Re=2000 than when Re=500.

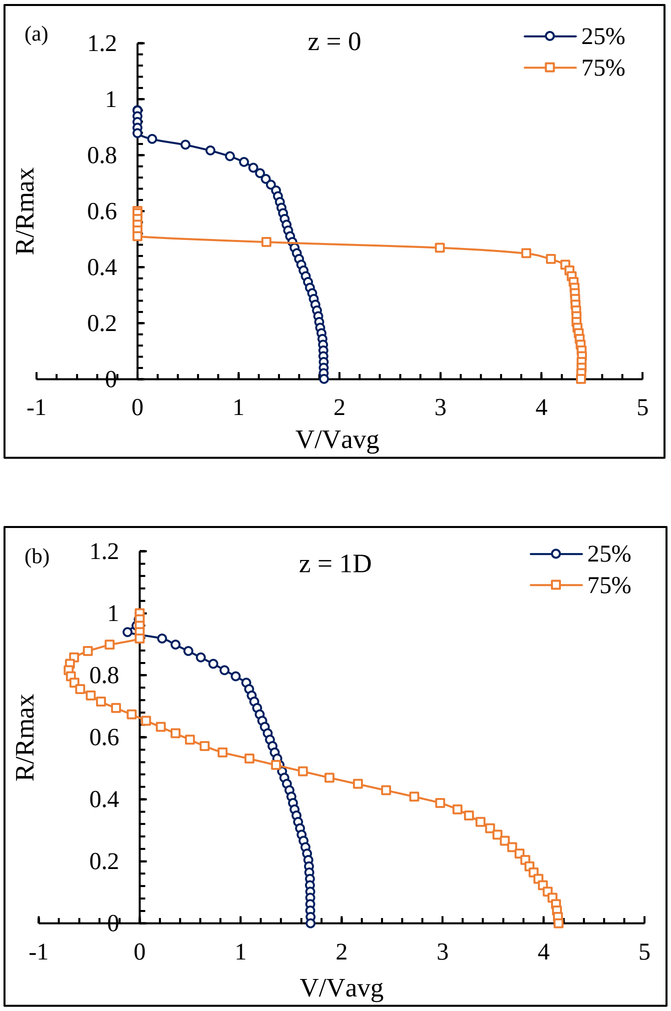

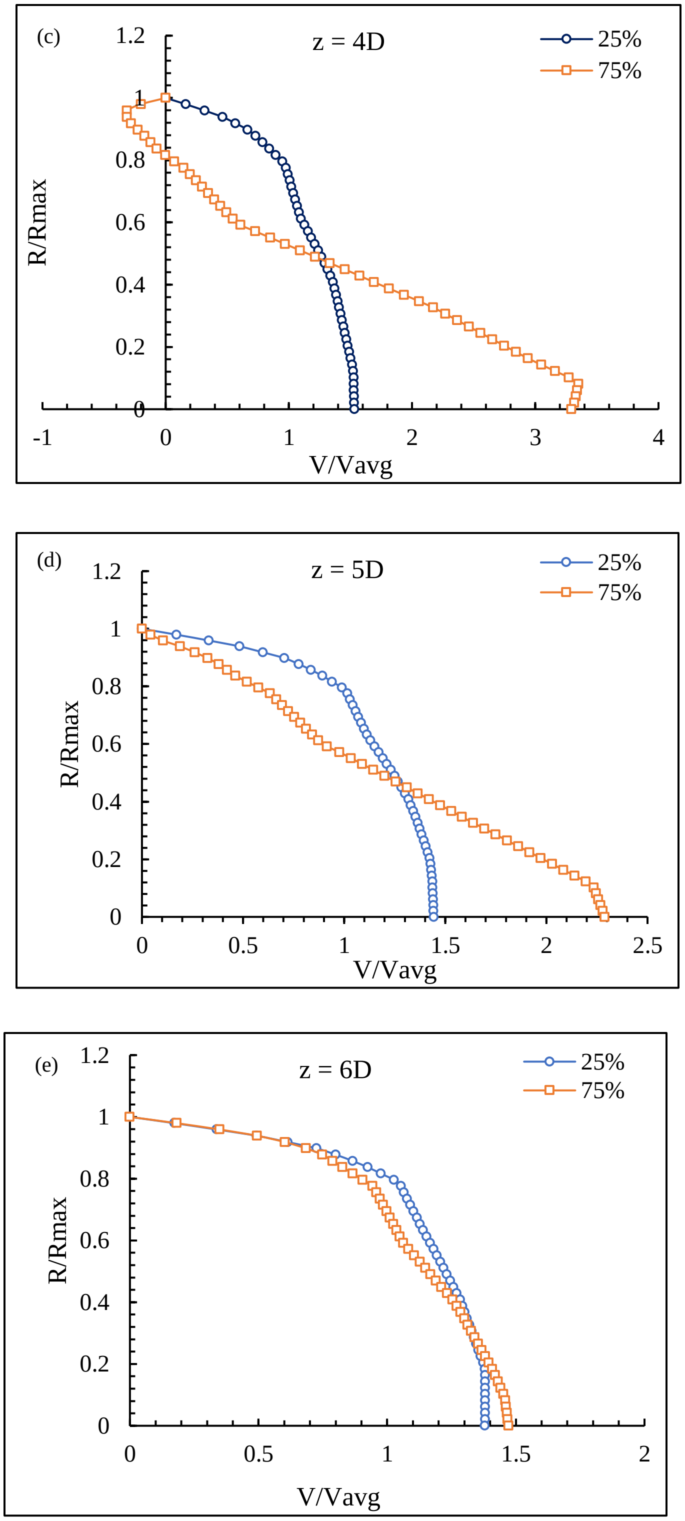

Figure 8. Dimensionless velocity profile for 25% and 75% stenosis at axial sites (a) *z* = 0, (b) *z* = 1*D*, (c) *z* = 4*D*, (d) *z* = 5*D*, (e) *z* = 6*D* at Re = 2000

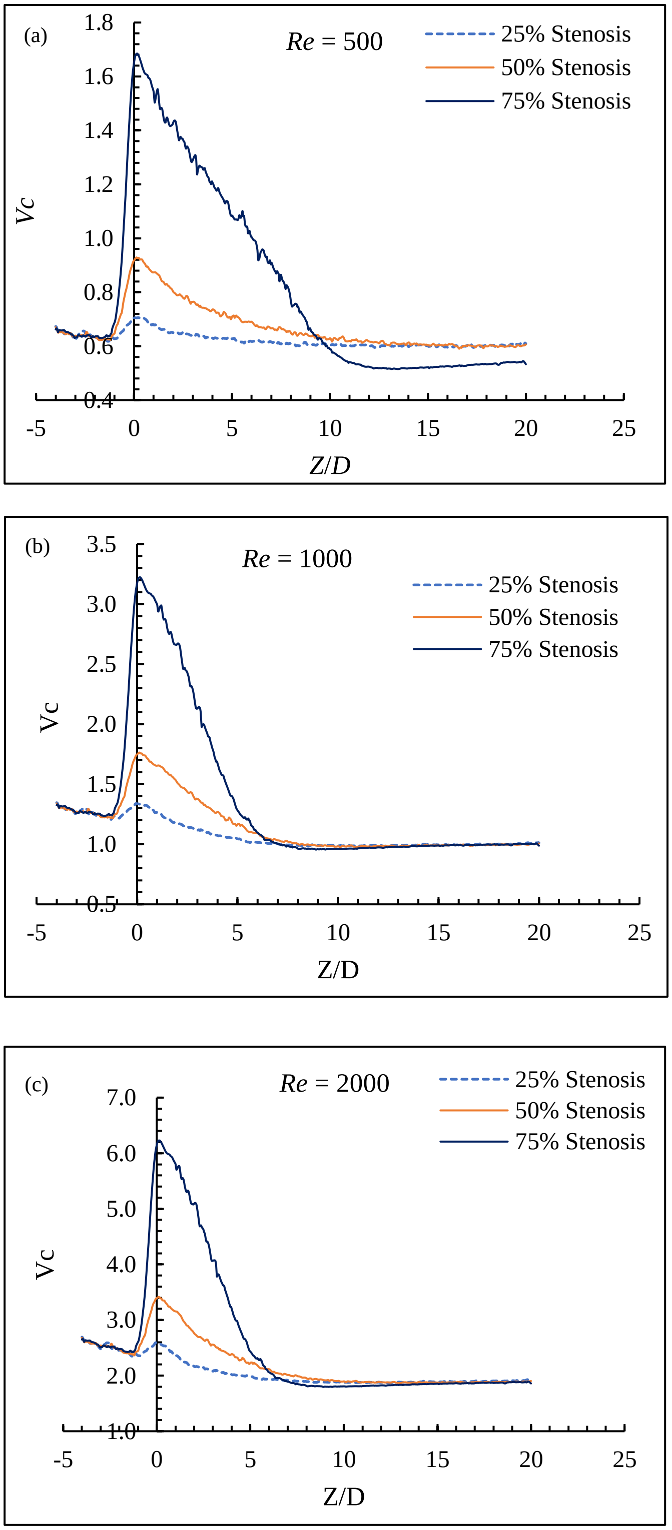

Figure 9. Comparisons of axial centerline velocity for 25%, 50% and 75% stenosis at Reynolds number (a) 500 (b)1000 (c)2000.

F. *Centreline Turbulence Intensity*

Figure 10 shows a comparison of the axial centerline turbulence intensity along a non-dimensional axial distance for 25%, 50% and 75% stenosis for Reynolds numbers 500, 1000, and 2000. The peak turbulence intensity increases with an increasing Reynolds number and degree of stenosis. As can be seen from Figure 10(a), for Re = 500, there is a sharp post-stenotic increase in disturbance intensity that is caused by the presence of discrete frequency velocity fluctuations rather than turbulence. For Re = 1000 and 2000, at the throat of the stenosis, the turbulence intensity increased quickly to a maximum, then went off more gradually until it eventually has fallen to a value equal to the upstream value. The findings show that the maximum intensity typically occurs close to the reattachment site. The transition into intense turbulence is responsible for the sharp increase in disturbance level. As shown in Figure 10b, a very mild flow disturbance difference along axial distance is observed in the 25% stenosis as well as indication of vortex shedding at z = 2.5D, which further decreases downstream of the stenosis. The peak value of intensity has a propensity to propagate upstream as the degree of stenosis rises at a fixed Re and as Re rises at a fixed percent of stenosis.

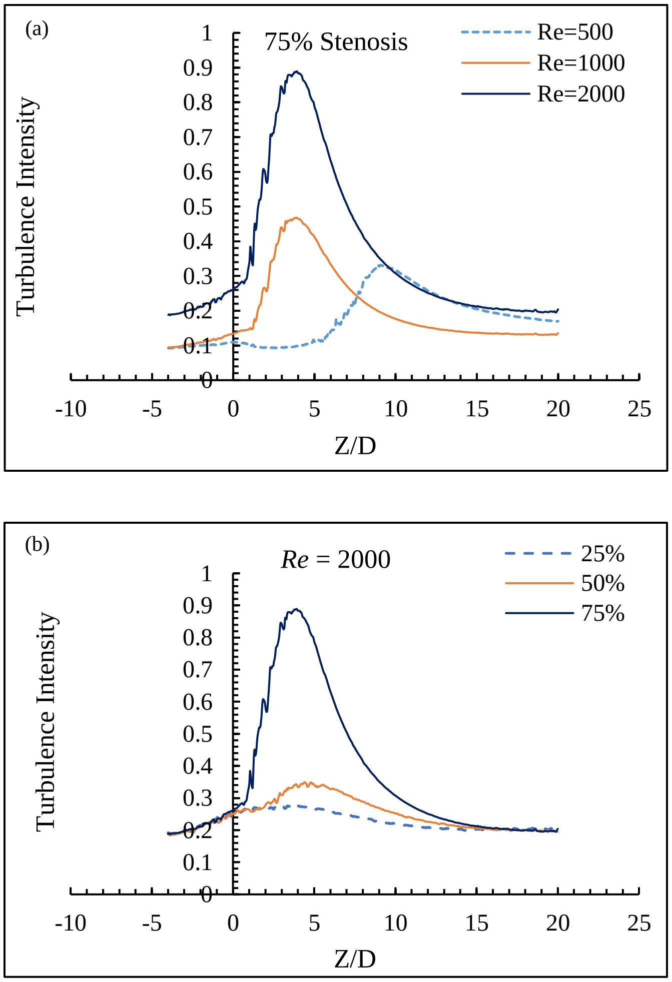

Figures 10. Comparisons of the centerline turbulence intensity (a) 75% at Reynolds number 500 (b) Reynolds number 2000 for 25%, 50% and 75%

G. *Axial Turbulence Intensity*

Figures 11 through 13 present variations of turbulence intensity along the axial site for 25%, 50%, and 75% stenosis, respectively at Reynolds numbers of 500, 1000, and 2000. Figure 11 shows that for the 25% stenosis, at all the aforementioned Reynolds numbers, no significant flow disturbances were evident. They all conformed with the experimental results reported in the work of (Ahmed and Giddens, 1983b). Figure 12, illustrates that for the case of 50% stenosis, no turbulence intensities were indicated at Re=500. Meanwhile, at Re=1000 a vortex shedding shear layer was noticed. Vortex shedding and flow disturbances were seen at the downstream of the constriction under the conditions of Re=2000. As presented in Figure 13, for the 75% stenosis, a flow disturbance was seen at all stated Reynolds numbers for this study, but somehow relatively blunt at Re=500. More so, at Re=500 a periodically oscillated shear layer was observed at axial site z=6D distal to the stenosis. Furthermore, at Re=1000 and 2000, both flow disturbance and vortex shedding were indicated.

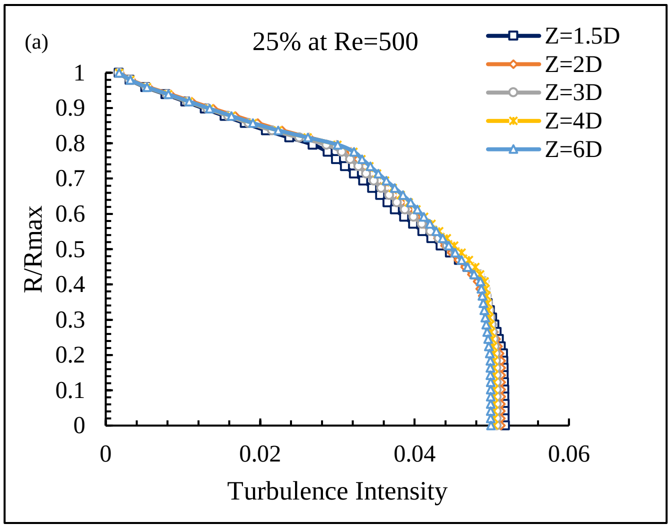

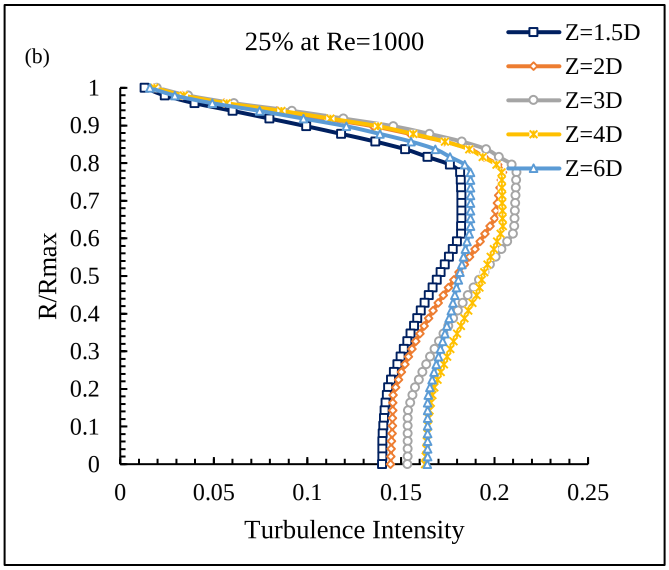

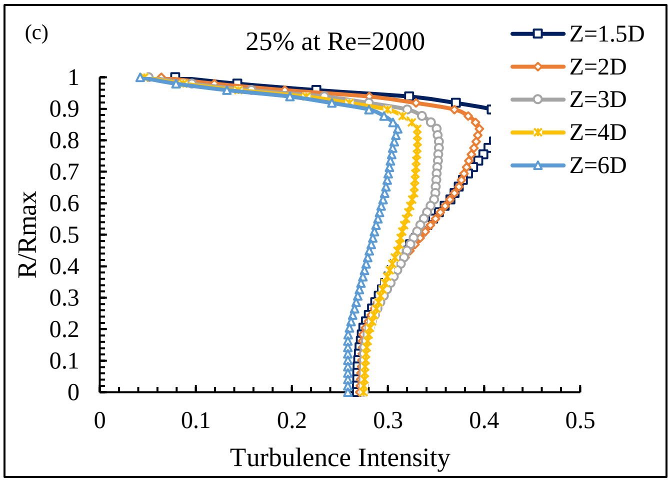

Figure 11. Variations of axial turbulence intensity for 25% stenosis at Reynolds number (a) 500 (b)1000 (c) 2000

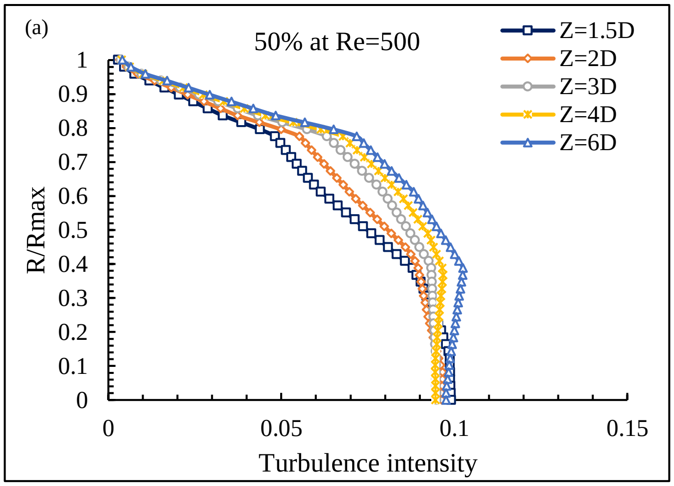

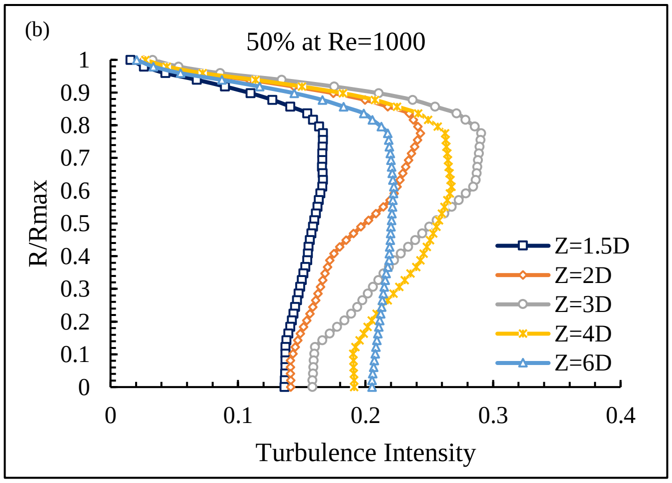

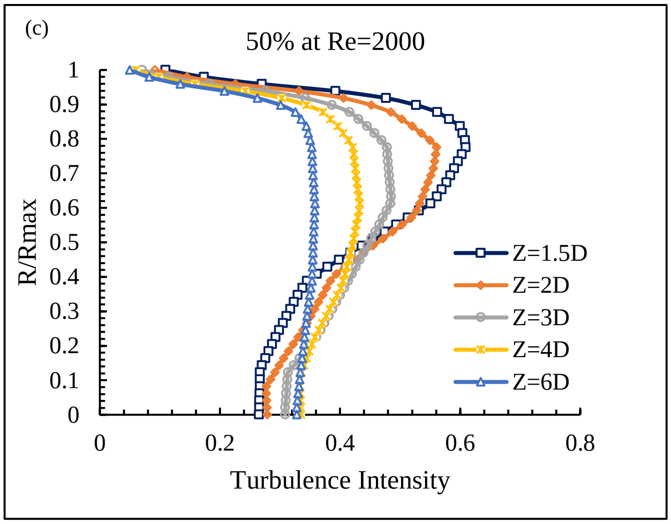

Figure 12. Variations of axial turbulence intensity for 50% stenosis at Reynolds number (a) 500 (b)1000 (c) 2000

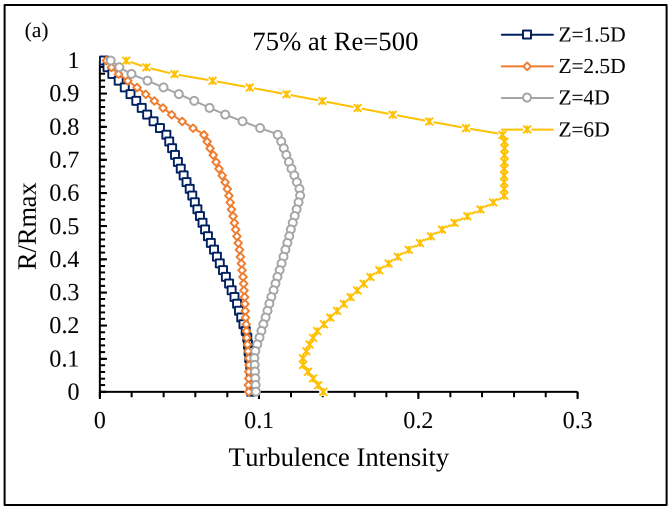

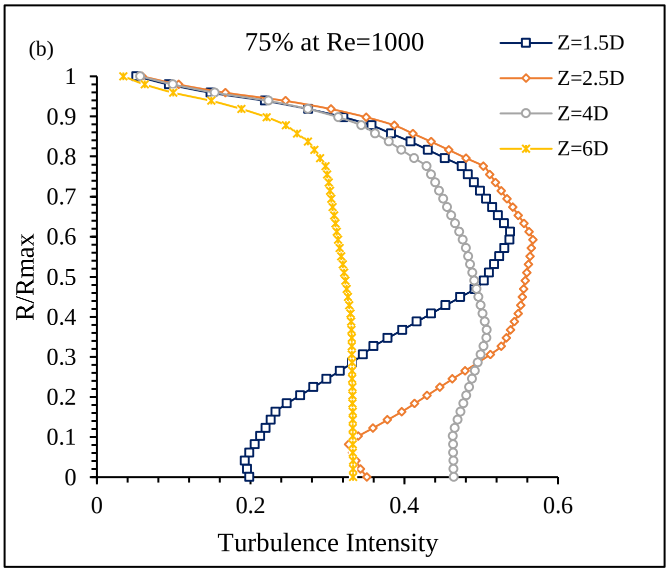

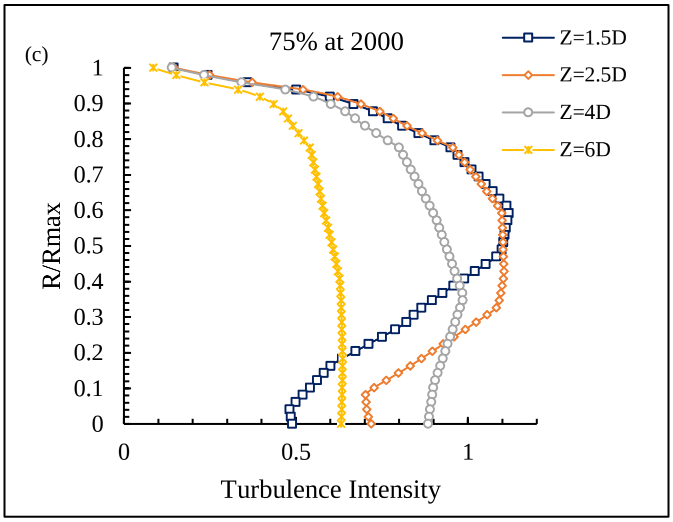

Figure 13. Variations of axial turbulence intensity for 75% stenosis at Reynolds number (a) 500 (b) 1000 (c) 2000.

H. Flow visualization

Flow visualization was adopted to gain a better insight into and understanding of the dynamic behavior of blood flow in the artery with stenosis. Figures 14 through 15 depict the velocity streamlines for 75%, 50% and 25% stenosis at Re= 2000 and Re=500. As can be observed in Figure 14 and Figure, for all cases of the stenosis, the formation of a jet is visible at the throat of the stenosis but fully developed in both 75% and 50% stenosis as compared to 25% stenosis. With the exception of 25% stenosis, flow recirculation is evident at the post-stenotic region in both 75% and 50% stenosis. The recirculation length zone is longer in the former than in the latter. Figure 16 and Figure 17 depict the turbulence intensity contours for 75%, 50% and 25% stenosis at Re= 2000 and Re=500, respectively. It can be evident in Figure 16, that highest magnitude of the turbulence intensity is reported at the post-stenotic site proximal to the stenosis. At this region, a pair of symmetric vortices which tend to reduce in size with the degree of the stenosis is also observed. As shown in Figure 17, vortices are distinctly present only when the stenosis reaches 75%, and their formation lacks symmetry at the post-stenotic site. These strongly suggest that both the degree of stenosis and the Reynolds number significantly influence the flow behavior, particularly in terms of flow pattern and vortex behavior, thereby influencing the overall flow characteristics. The degree of stenosis directly affects the flow passage's narrowing, while the Reynolds number reflects the balance between inertial and viscous forces in the fluid. The visual evidence of vortices exclusively in the 75% stenosis scenario implies that the severity of the flow restriction plays a critical role in the generation of vortical structures. Additionally, the lack of symmetry in vortex formation at the post-stenotic region suggests that the stenosis induces irregular flow patterns, leading to asymmetrical vortex development.

Vortices are distinctly present only when the stenosis reaches 75%, and their formation lacks symmetry at the post-stenotic site. These findings strongly suggest that both the degree of stenosis and the Reynolds number significantly influence the flow behavior, particularly in terms of flow disturbance and vortex formation.

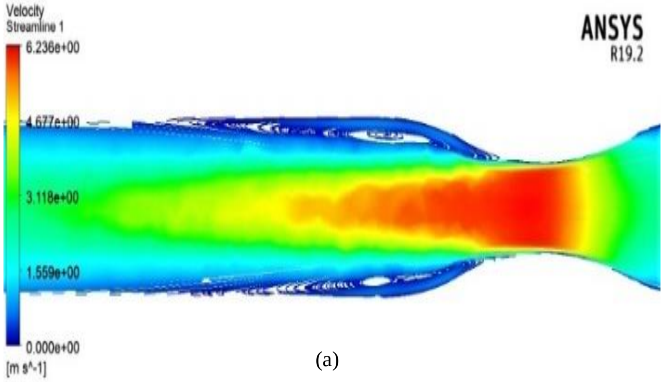

(a)

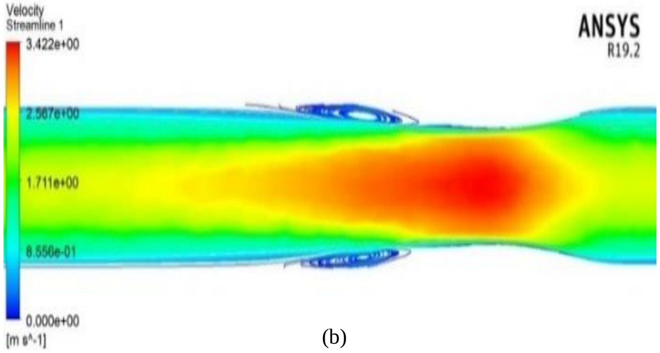

(b)

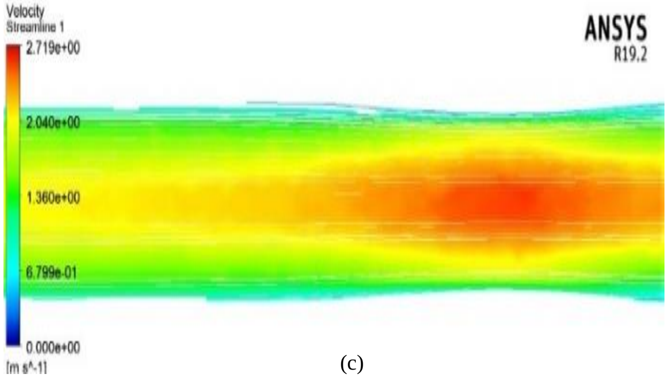

(c)

Figure 14. Velocity streamline at Re=2000 for (a) 75% (b) 50% (c) 25% stenosis

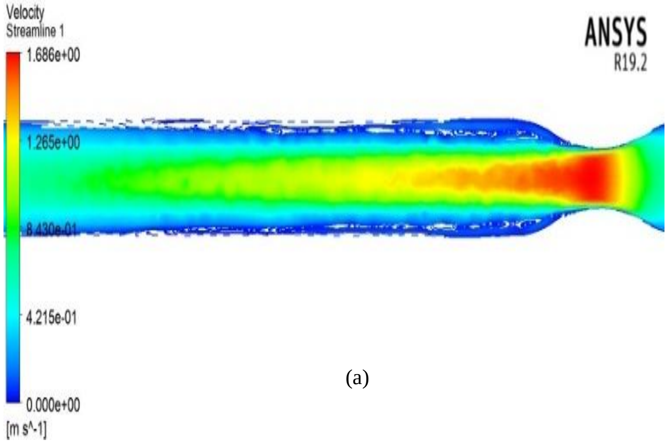

(a)

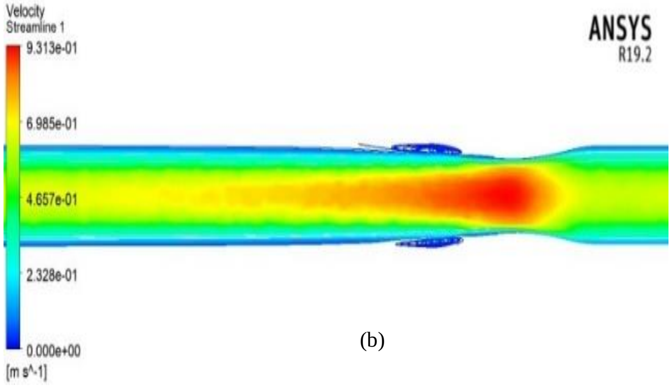

(b)

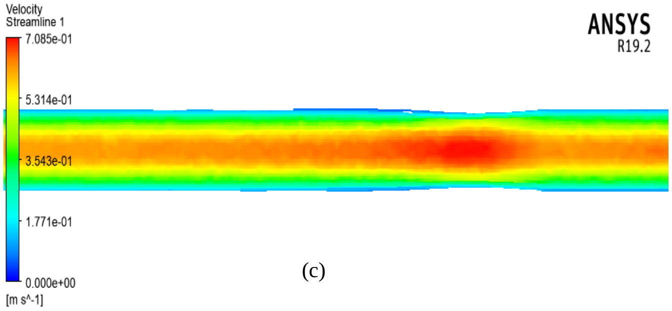

(c)

Figure 15. Velocity streamline at Re=500 for (a) 75% (b) 50% (c) 25% stenosis

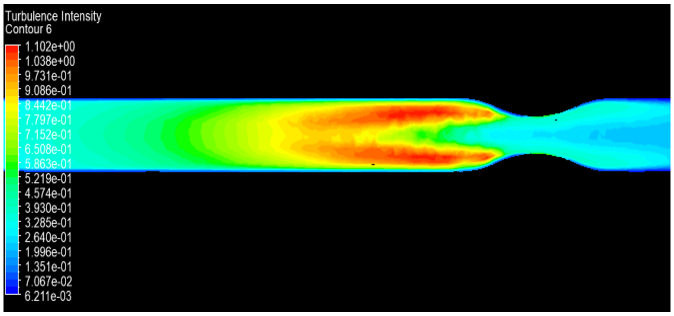

(a)

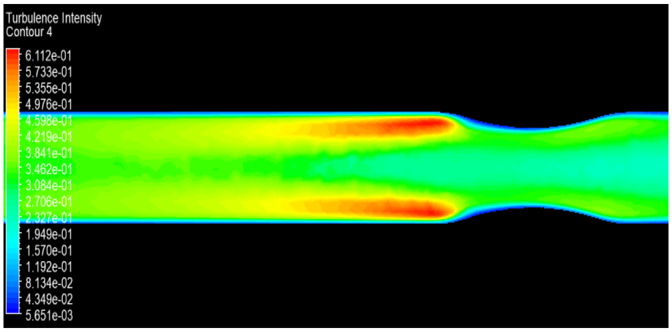

(b)

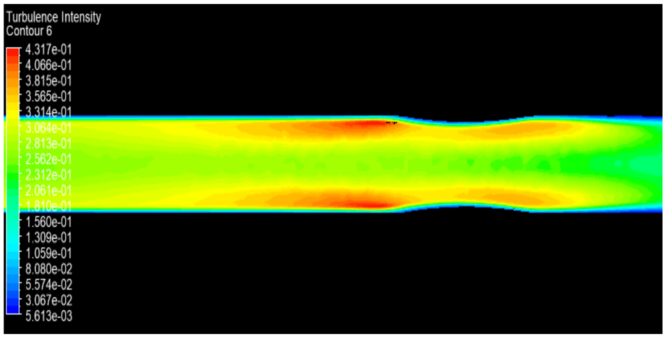

(c)

Figure 16. Turbulence intensity contour at Re=2000 for (a) 75% (b) 50% (c) 25% stenosis

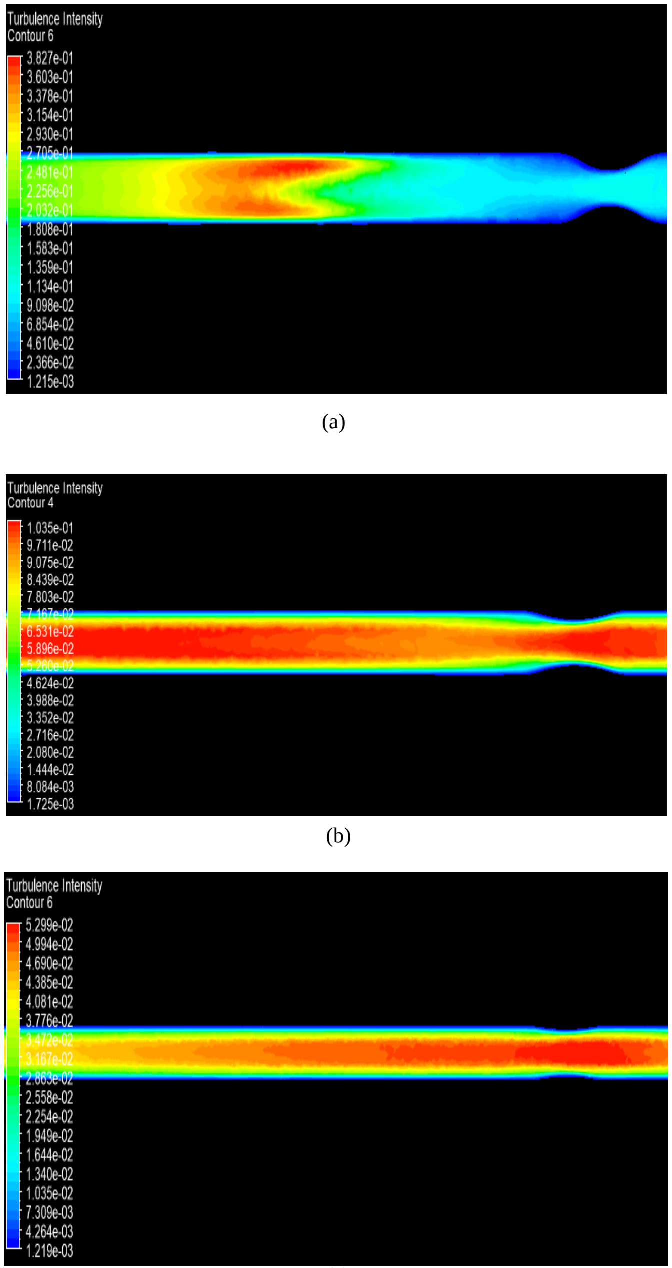

(a)

(b)

(c)

Figure 17. Turbulence intensity contour at Re=500 for (a) 75% (b) 50% (c) 25% stenosis

V. CONCLUSION

In conclusion, this rigorous computational investigation on steady blood flow through stenotic arteries has provided crucial insights into the impact of stenosis severity on key hemodynamic indicators. The research findings present significant contributions to the understanding of cardiovascular biomechanics, and the following salient conclusions can be drawn from this study:

1. The presence of a distinct recirculation zone in the post-stenotic region was evident for 50% and 75% stenosis cases, whereas such phenomena were conspicuously absent in the 25% stenosis scenario. This nuanced distinction implies that moderate and severe stenosis levels are more prone to inducing flow disturbances and recirculation patterns within the artery.
2. The evidence of a shear layer downstream of the stenosis, resulting from flow obstruction due to area reduction, triggered adverse pressure gradients and subsequent flow separation. This fluid dynamics phenomenon is particularly pronounced in cases of higher stenosis severity such as 75% stenosis.
3. The region near or at the throat of the stenosis exhibited predominantly laminar flow characteristics, as evidenced by critical analysis of turbulence intensity. This indicates a relatively stable and predictable flow pattern in this vicinity.
4. Crucially, the investigation revealed a notable escalation in centerline velocity and turbulence levels at the throat region with an increase in stenosis severity across all Reynolds number cases. This underscores the pivotal role of severe stenosis in significantly influencing flow dynamics and potentially elevating the risk of deleterious cardiovascular events.
5. Moreover, 75% stenosis significantly alters flow patterns, inducing flow separation, recirculation, and jet formation, with potential adverse cardiovascular effects. In contrast, 25% stenosis shows a milder impact on flow patterns, indicating less disruption to arterial hemodynamics.

REFERENCES

Ahmed, S.A. and Giddens, D.P. (1983a). Velocity measurements in steady flow through axisymmetric stenoses at moderate Reynolds numbers. Journal of Biomechanics, 16(7): 505–516. https://doi.org/10.1016/0021-9290(83)90065-9.

Ahmed, S.A. and Giddens, D.P. (1983b). Velocity measurements in steady flow through axisymmetric stenoses at moderate Reynolds numbers. Journal of Biomechanics, 16(7): 505–516. https://doi.org/10.1016/0021-9290(83)90065-9.

Ahmed, S.A. and Giddens, D.P. (1984). Pulsatile poststenotic flow studies with laser Doppler anemometry. Journal of Biomechanics, 17(9): 695–705. https://doi.org/10.1016/0021-9290(84)90123-4.

Albadawi, M.; Y. Abuouf; S. Elsagheer; S. Ookawara and M. Ahmed. (2021). Predicting the onset of consequent stenotic regions in carotid arteries using computational fluid dynamics. Physics of Fluids, 33(12). https://doi.org/10.1063/5.0068998/1062060.

Albadawi, M.; Y. Abuouf; S. Elsagheer; H. Sekiguchi; S. Ookawara and M. Ahmed. (2023). Is the Blood Flow Laminar or Turbulent at Stenosed Coronary Artery?. ASME International Mechanical Engineering Congress and Exposition. Proceedings (IMECE), 4. https://doi.org/10.1115/IMECE2022-95594.

Amir, M.; A.Y. Usmani; M. Varshney; S.F. Anwer; S.A. Khan; N. Islam and A.A. Pasha. (2022). Analysing Spatio-temporal flow hemodynamics in an artery manifesting stenosis. International Journal of Mechanical Sciences, 218, 107072. https://doi.org/10.1016/J.IJMECSCI.2022.107072.

Banks, J. and Bressloff, N.W. (2007). Turbulence Modeling in Three-Dimensional Stenosed Arterial Bifurcations. Journal of Biomechanical Engineering, 129(1): 40–50. https://doi.org/10.1115/1.2401182.

Changsheng, L.; F. Haiquan; W. Kun; W. Xiaotian and W. Yonggang. (2023). Influence of the Anatomical Structure on the Hemodynamics of Iliac Vein Stenosis. Journal of biomechanical engineering, 145(1). https://doi.org/10.1115/1.4055307/1145735.

Dabagh, M.; P. Vasava and P. Jalali. (2015). Effects of severity and location of stenosis on the hemodynamics in human aorta and its branches. Medical and Biological Engineering and Computing, 53(5): 463–476. https://doi.org/10.1007/S11517-015-1253-3/METRICS.

Deshpande, M.D.; D.P. Giddens and R.F. Mabon. (1976). Steady laminar flow through modelled vascular stenoses. Journal of Biomechanics, 9(4) 165–174. https://doi.org/10.1016/0021-9290(76)90001-4.

Dietiker, J.F. and Hoffmann, K.A. (2006). Computation of three-dimensional blood flows in arteries. Collection of Technical Papers - 36th AIAA Fluid Dynamics Conference, 2, 797–811. https://doi.org/10.2514/6.2006-3213.

Ferdows, M.; K.E. Hoque; M.Z.I. Bangalee and M.A. Xenos. (2023). Wall shear stress indicators influence the regular hemodynamic conditions in coronary main arterial diseases: cardiovascular abnormalities. Computer Methods in Biomechanics and Biomedical Engineering, https://doi.org/10.1080/10255842.2022.2054660, 26(2): 235–248.

Hoque, K.E.; M. Ferdows; S. Sawall; E.E. Tzirtzilakis and M.A. Xenos. (2021). The impact of hemodynamic factors in a coronary main artery to detect the atherosclerotic severity: Single and multiple sequential stenosis cases. Physics of Fluids, 33(3): https://doi.org/10.1063/5.0041335/1063791.

World Health Organization. 2009. Cardiovascular diseases (cvds). http://www. who. int/mediacentre/factsheets/fs317/en/index. html.

Liao, W.; T.S. Lee and H.T. Low. (2011). Numerical study of physiological turbulent flows through stenosed arteries. International Journal of Modern Physics C, 14(05): 635-659. https://doi.org/10.1142/S0129183103004838.

Mirfendereski, S. and Park, J.S. (2022). Direct numerical simulation of a pulsatile flow in a stenotic channel using immersed boundary method. Engineering Reports, 4(1): 12444. https://doi.org/10.1002/ENG2.12444.

Mittal, R.; S.P. Simmons and F. Najjar. (2003). Numerical study of pulsatile flow in a constricted channel. Journal of Fluid Mechanics, 485: 337–378. https://doi.org/10.1017/S002211200300449X.

Molochnikov, V.M.; A.N. Mikheev; A.B. Mazo; E.I. Kalinin; M.A. Klyuev and N.D. Pashkova. (2022). Structure of the proximal anastomosis flow in stationary mode at moderate Reynolds numbers. Thermophysics and Aeromechanics, 29(6): 905–911. https://doi.org/10.1134/S0869864322060105/METRICS.

Ryval, J.; A.G. Straatman and D.A. Steinman. (2004). Two-equation Turbulence Modeling of Pulsatile Flow in a Stenosed Tube. Journal of Biomechanical Engineering, 126(5): 625–635. https://doi.org/10.1115/1.1798055.

Varghese, S.S.; S.H. Frankel and P.F. Fischer. (2007a). Direct numerical simulation of stenotic flows. Part 1. Steady flow. Journal of Fluid Mechanics, 582: 253–280. https://doi.org/10.1017/S0022112007005848.

Varghese, S.S.; S.H. Frankel and P.F. Fischer. (2007b). Direct numerical simulation of stenotic flows. Part 2. Pulsatile flow. Journal of Fluid Mechanics, 582: 281–318. https://doi.org/10.1017/S0022112007005836.

Zhao, Y.C.; P. Vatankhah; T. Goh; R. Michelis; K. Kyanian; Y. Zhang; Z. Li and L.A. Ju. (2021). Hemodynamic analysis for stenosis microfluidic model of thrombosis with refined computational fluid dynamics simulation. Scientific Reports, 11(1): 1–10. https://doi.org/10.1038/s41598-021-86310-2.